The Astrophysical Journal Letters, 973:L11 (14pp), 2024 September 20 https://doi.org/10.3847/2041-8213/ad74ed

The MIRI Exoplanets Orbiting White dwarfs (MEOW) Survey: Mid-infrared Excess Reveals a Giant Planet Candidate around a Nearby White Dwarf

Mary Anne Limbach[1], Andrew Vanderburg[2], Alexander Venner[3], Simon Blouin[4], Kevin B. Stevenson[5], Ryan J. MacDonald[1,16], Sydney Jenkins[2], Rachel Bowens-Rubin[1], Melinda Soares-Furtado[6,17], Caroline Morley[7], Markus Janson[8], John Debes[9], Siyi Xu[10], Evangelia Kleisioti[11,12], Matthew Kenworthy[11], Paul Butler[13], Jeffrey D. Crane[14], Dave Osip[15], Stephen Shectman[14], and Johanna Teske[13]

[1] Department of Astronomy, University of Michigan, Ann Arbor, MI 48109, USA; mlimbach@umich.edu
[2] Department of Physics and Kavli Institute for Astrophysics and Space Research, Massachusetts Institute of Technology, Cambridge, MA 02139, USA
[3] Centre for Astrophysics, University of Southern Queensland, Toowoomba, QLD 4350, Australia
[4] Department of Physics and Astronomy, University of Victoria, Victoria, BC V8W 2Y2, Canada
[5] Johns Hopkins APL, 11100 Johns Hopkins Road, Laurel, MD 20723, USA
[6] Department of Astronomy, University of Wisconsin–Madison, 475 North Charter Street, Madison, WI 53706, USA
[7] Department of Astronomy, University of Texas at Austin, Austin, TX, USA
[8] Department of Astronomy, Stockholm University, AlbaNova University Center, 10691 Stockholm, Sweden
[9] AURA for the European Space Agency (ESA), ESA Office, Space Telescope Science Institute, 3700 San Martin Drive, Baltimore, MD 21218, USA
[10] Gemini Observatory/NSF's NOIRLab, 670 North A'ohoku Place, Hilo, HI 96720, USA
[11] Leiden Observatory, Leiden University, PO Box 9513, 2300 RA Leiden, The Netherlands
[12] Aerospace Engineering, TU Delft, Building 62 Kluyverweg 1, 2629 HS Delft, The Netherlands
[13] Earth and Planets Laboratory, Carnegie Institution for Science, 5241 Broad Branch Road, NW, Washington, DC 20015, USA
[14] The Observatories of the Carnegie Institution for Science, 813 Santa Barbara Street, Pasadena, CA 91101, USA
[15] Las Campanas Observatory, Carnegie Institution for Science Colina el Pino, Casilla 601 La Serena, Chile

Received 2024 August 9; revised 2024 August 27; accepted 2024 August 28; published 2024 September 19

Abstract

The MIRI Exoplanets Orbiting White dwarfs survey is a cycle 2 JWST program to search for exoplanets around dozens of nearby white dwarfs via infrared excess and direct imaging. In this Letter, we present the detection of mid-infrared excess at 18 and 21 μm toward the bright ($V = 11.4$) metal-polluted white dwarf WD 0310–688. The source of the IR excess is almost certainly within the system; the probability of background contamination is <0.1%. While the IR excess could be due to an unprecedentedly small and cold debris disk, it is best explained by a $3.0^{+5.5}_{-1.9}\ M_{\rm Jup}$ cold (248^{+84}_{-61} K) giant planet orbiting the white dwarf within the forbidden zone (the region where planets are expected to be destroyed during the star's red giant phase). We constrain the source of the IR excess to an orbital separation of 0.1–2 au, marking the first discovery of a white dwarf planet candidate within this range of separations. WD 0310–688 is a young remnant of an A- or late B-type star, and at just 10.4 pc, it is now the closest white dwarf with a known planet candidate. Future JWST observations could distinguish the two scenarios by either detecting or ruling out spectral features indicative of a planet atmosphere.

Unified Astronomy Thesaurus concepts: Infrared excess (788); Extrasolar gaseous giant planets (509); White dwarf stars (1799); Debris disks (363); Exoplanet migration (2205)

1. Introduction

White dwarfs represent the final evolutionary stage for most stars, including our Sun. Despite this common endpoint, the fate of their planetary systems remains poorly understood. Detection of exoplanets around white dwarfs has been challenging using traditional methods suitable for main-sequence stars (M. Endl & K. Williams 2018; W. Zhu & S. Dong 2021). To date, only a few white dwarf exoplanets have been confirmed.

Due to the limited number of known white dwarf planets, we lack a comprehensive understanding of planetary evolution during the white dwarf phase. Increased detections could facilitate demographic studies and detailed characterization of such systems (J. H. Debes et al. 2005; D. Veras 2021; S. Ledda et al. 2023; S. Poulsen et al. 2024). This knowledge could help us ascertain whether planets can endure the death of their host stars and remain in orbit around the resultant white dwarf, as well as identify the conditions under which planets might be disrupted or destroyed during the red giant phase (J. H. Debes & S. Sigurdsson 2002; B. Zuckerman et al. 2010). Furthermore, a deeper understanding of white dwarf planetary systems could reveal whether life can arise around dead stars (E. Agol 2011; L. Fossati et al. 2012; R. Barnes & R. Heller 2013; A. Loeb & D. Maoz 2013; T. Kozakis et al. 2018, 2020; J. Becker et al. 2023; R. Zhan et al. 2024).

The near-featureless infrared spectrum of white dwarfs is a valuable characteristic for exoplanet searches using the detection of infrared excess, which can indicate the presence of sources colder than the white dwarf within the system, such as debris disks, late-type stellar companions, brown dwarfs, or exoplanets (E. E. Becklin et al. 2005; M. Kilic et al. 2005; J. Farihi et al. 2008b; S. D. Barber et al. 2012; K. B. Stevenson 2020; M. A. Limbach et al. 2022). The IR excess technique enabled the discovery of the first brown dwarf–white dwarf system (B. Zuckerman & E. E. Becklin 1987; T. Cunningham et al. 2022) and has since been employed to identify numerous

---

[16] NHFP Sagan Fellow.
[17] NASA Hubble Science Fellow.

similar systems (e.g., J. Girven et al. 2011; S. Xu et al. 2015; A. Rebassa-Mansergas et al. 2019; M. A. Hogg et al. 2020; S. Lai et al. 2021). Although the Spitzer Space Telescope was used in attempts to detect exoplanet-induced IR excess in white dwarf systems (M. W. Werner et al. 2004; F. Mullally et al. 2007; J. Farihi et al. 2008a; M. Kilic et al. 2010), no candidates were identified.

Fortunately, with the advent of the JWST, our ability to detect exoplanets around white dwarfs has drastically improved. JWST has multiple programs designed to detect new white dwarf exoplanets (S. E. Mullally et al. 2021; M. A. Limbach et al. 2023; S. Poulsen et al. 2023). These search programs have resulted in the detection of multiple candidates (S. E. Mullally et al. 2024b; this work), and follow-up observations to confirm planet candidates are underway (A. Venner et al. 2023; S. Cheng et al. 2024; F. Mullally et al. 2024a). JWST's capabilities also extend to characterizing known white dwarf exoplanets (R. J. MacDonald et al. 2021; A. Vanderburg et al. 2021; J. Blackman et al. 2024; M. A. Limbach et al. 2024).

Despite these impressive advancements, no known exoplanets (confirmed or candidate) exist around white dwarfs at midseparations (0.1–2 au). Depending on the mass of the star, exoplanets beyond ∼2 au are expected to survive the final stages of stellar evolution intact (J. Nordhaus & D. S. Spiegel 2013). Discovering planets near or inward of this anticipated boundary illuminates our understanding of post-main-sequence exoplanet evolution and migration. The recent discovery of a volatile-rich gaseous debris disk from an evaporating giant planet (B. T. Gänsicke et al. 2019) and the discovery of a gas giant exoplanet orbiting at only 0.02 au (A. Vanderburg et al. 2020) suggest that massive planets may find their way into tight orbits around white dwarfs, and the discovery of dusty disks (generally hotter than giant planets but colder than the white dwarf) around about 2%–3% of white dwarfs indicates that large rocky bodies may be torn apart by gravitational tides, producing a closely orbiting hot dust disk. The only other known white dwarf exoplanets and planet candidates orbit beyond the 2 au boundary where survival is expected (S. E. Thorsett et al. 1993; S. Sigurdsson et al. 2003; K. L. Luhman et al. 2011; J. W. Blackman et al. 2021; S. E. Mullally et al. 2024b).

The detection of exoplanets around metal-polluted white dwarfs presents a unique opportunity to explore the intricate dynamics between stellar remnants and planetary systems. Metal-rich white dwarfs are characterized by the presence of heavier elements in their atmospheres. This is surprising because metals should rapidly settle (on timescales as fast as days for hydrogen envelope white dwarfs; D. Koester & D. Wilken 2006; M. Kilic et al. 2006; M. Jura et al. 2007; D. Koester 2009) below the white dwarf's surface due its strong gravitational fields, leaving only lightweight elements like hydrogen and helium in the atmosphere. Therefore, the presence of metals in white dwarf atmospheres indicates that they are likely undergoing recent or active accretion. Studies in recent decades have concluded that the source of this accretion (also referred to as pollution) is usually minor planets, comets, and asteroids from the progenitor system that survived red giant evolution (C. Alcock et al. 1986; M. Jura 2003; P. Dufour et al. 2010; B. Klein et al. 2010; J. H. Debes et al. 2012; D. Veras et al. 2024). They likely moved close to the white dwarf due to gravitational interactions with other massive bodies, such as giant planets, in the system. Small bodies, once destabilized, can migrate inward and eventually cross the white dwarf's Roche limit, where they are tidally disrupted into dust and gas. This debris, rich in metals, then accretes onto the white dwarf, polluting its atmosphere. The chemical fingerprints of these accreted materials closely mirror the composition of terrestrial planets, such as Earth, providing strong evidence for this model (C. Melis et al. 2011; S. Xu et al. 2019; I. L. Trierweiler et al. 2023).

Discovering white dwarf systems with planets and disks is crucial to validating the current theories on white dwarf accretion and planetary survival post-main-sequence. In this Letter, we present the detection of infrared excess at <2 au around the metal-polluted white dwarf WD 0310–688. Our observations, conducted as part of the MIRI Exoplanets Orbiting White dwarfs (MEOW) JWST survey program, are detailed in Section 2. Section 3 covers our analysis of the MEOW data, focusing on the detection of infrared excess in the WD 0310–688 system. We use our MEOW data, modeling, and archival data to constrain the source of infrared excess and its physical parameters. In Section 4, we discuss the implications of this detection and outline how future observations could confirm the source as an exoplanet. Finally, we summarize our findings in Section 5.

2. Observations

The MEOW survey is a JWST Cycle 2 survey program (analogous to Hubble Space Telescope, HST, "snapshot" programs) to collect three-band MIRI imaging of ∼20 nearby white dwarfs in search of exoplanets. Utilizing a combination of infrared excess and direct imaging techniques, the MEOW survey is capable of detecting white dwarf exoplanets at all separations, from the Roche limit to the edge of the field of view (∼1000 au; depending on the exact distance to the system). MEOW is sensitive to extremely cold planets, with the ability to detect exoplanets with masses as low as that of Saturn and temperatures down to 120 K for the youngest, nearest systems and planets with temperatures as low as 175 K, equivalent to a 2 $M_{\rm Jup}$ at 3 Gyr, out to a distance of 16 pc.

The MEOW survey is volume-limited (<17 pc). It includes solitary white dwarfs and white dwarfs with faint companions (main-sequence stars later than M4V or binary white dwarfs). White dwarfs with bright main-sequence companions (e.g., Sirius B, Procyon B, 40 Eridani B, etc.) are excluded, as a different imaging configuration would be optimal for detecting exoplanets in those systems.

Imaging is taken in three MIRI bands: F770W, F1800W, and F2100W (7.7, 18.0, and 21.0 μm, respectively). For the F770W filter, our total exposure time is 55.5 s (five groups/int, one int/exp), which is sufficient to achieve a signal-to-noise ratio (SNR) >200 on all targets in our sample while still avoiding saturation on the nearest white dwarfs. The SNR in the 7.7 μm band is dominated by photon noise from the target star; however, our absolute photometric precision is limited to 2% by the absolute flux calibration of the MIRI imager[18] (K. D. Gordon et al. 2022). For the F1800W and F2100W filters, our exposure times are 277.5 s and 710.4 s, respectively (12 groups/int, two or five int/exp), which results in an SNR between 10 and 125 on all targets in our sample. Depending on

---

[18] jwst-docs.stsci.edu/jwst-data-calibration-considerations/jwst-data-absolute-flux-calibration

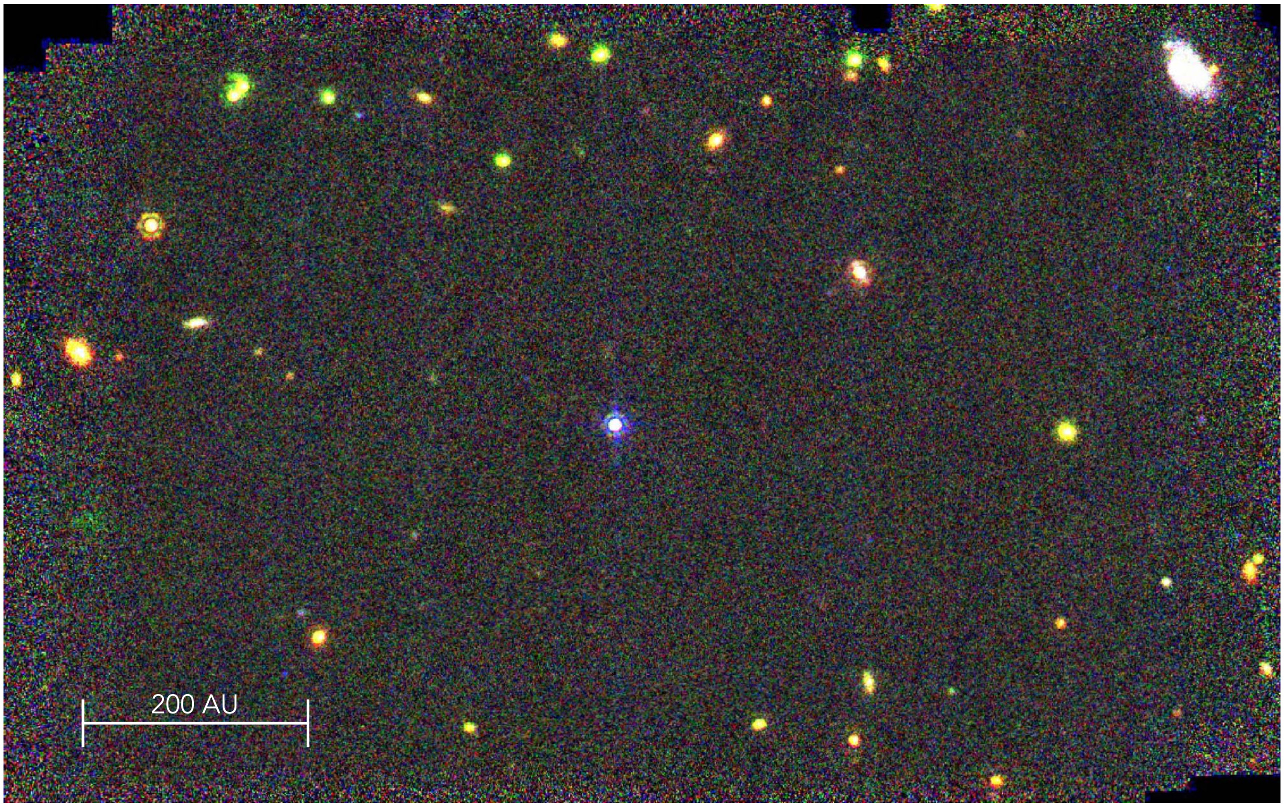

Figure 1. False-color image of WD 0310–688 (bluish-white star in the center) using three JWST/MIRI bands: F770W (blue), F1800W (green), and F2100W (red). Other sources in the field include distant galaxies, background stars, and potentially a few point sources that could be wide-orbit exoplanets bound to WD 0310–688. Although not the main focus of this Letter, we note the very faint source 80 au above the white dwarf, which is marginally detected at 18 and 21 μm, consistent with a $T_{\rm eff} \sim 140$ K planet slightly less massive than Jupiter; however, at this separation, the false-positive rate is reasonably high. Confirming any resolved sources as bound exoplanets would necessitate follow-up observations for common proper motion at a later epoch.

the target brightness, the noise in the 18 and 21 μm bands can be dominated by either the thermal background noise or the 2% absolute photometric precision.

For all imaging, we used the fast readout mode and a four-point cycling dither (starting point 1). We chose a four-point cycling dither to correct for bad pixels and remove background noise. We used the full MIRI imaging array, which has a $74'' \times 113''$ usable field of view, and a detector plate scale of $0\overset{''}{.}11$ pixel^{-1} (P. Bouchet et al. 2015).

The observations of WD 0310–688 began at 2023 September 19 22:50:31 UT and ended at 2023 September 19 23:53:06, about 1 hr later.[19] The false-color image constructed from the MIRI imaging in the three bands is shown in Figure 1.

Some initial findings from the MEOW survey are included in this Letter, as they relate to the infrared excess detected around WD 0310–688. However, the majority of the survey's results and analysis will be detailed in a future manuscript. This Letter primarily focuses on reporting the discovery of a planet candidate around WD 0310–688.

3. Analysis

3.1. The White Dwarf WD 0310–688

WD 0310–688 is a solitary white dwarf located at a distance of 10.4 pc. With V- and G-band magnitudes of 11.4 mag, it is the fifth-brightest white dwarf at visible wavelengths and the single brightest solitary white dwarf in the sky.[20]

3.1.1. Stellar Parameters

The spectroscopic (A. Bédard et al. 2017) and photometric (N. P. Gentile Fusillo et al. 2021) determinations of WD 0310–688's atmospheric parameters differ slightly, so we calculate the ages based on both sets of parameters. This white dwarf is in a regime where a small difference in its mass can significantly affect its main-sequence lifetime. We calculated the white dwarf parameters using `wdwarfdate`, and the resulting parameters are listed in Table 1. These parameters suggest that the host is a remnant of an A or late B star. We base our calculations on photometric white dwarf parameters because the spectroscopic parameters yield a slightly low white dwarf flux that is in tension with Gaia photometry, thus favoring the photometric solution. The photometric parameters give a white dwarf mass of $0.659 \pm 0.012\,M_\odot$ and cooling age of 194 ± 13 Myr.

3.1.2. Metal Lines and Accretion

WD 0310–688 is classified in the literature as a hydrogen-atmosphere (DA) white dwarf with no metal lines and has been observed as part of ground-based observation campaigns (D. Koester et al. 2009). However, in a previously unpublished

---

[19] Of note, this star was the very first JWST survey observation ever conducted, for any survey program.

[20] The five brightest white dwarfs in the optical are Sirius B ($V = 8.4$), 40 Eri B ($V = 9.5$), Procyon B ($V = 10.9$), CD-38 10980 ($V = 11.0$), and WD 0310–688 ($V = 11.4$) (J. B. Holberg et al. 2008; N. P. Gentile Fusillo et al. 2021).

Table 1
WD 0310–688 Spectroscopic and Photometric Derived Parameters

Parameter	Spectroscopic[a]	Photometric[b]
$T_{\rm eff}$ (K)	16,246 ± 237	15,865 ± 263
$\log(g)$	8.14 ± 0.04	8.076 ± 0.020
Initial mass ($M_\odot$)	$2.3^{+0.4}_{-0.5}$	1.9 ± 0.4
Main-sequence lifetime (Gyr)	$0.9^{+0.6}_{-0.3}$	$1.4^{+1.4}_{-0.5}$
Total age (Gyr)	$1.1^{+0.6}_{-0.3}$	$1.6^{+1.4}_{-0.5}$

Notes.
[a] Spectroscopic $T_{\rm eff}$ and $\log(g)$ from A. Bédard et al. (2017).
[b] Photometric $T_{\rm eff}$ and $\log(g)$ from N. P. Gentile Fusillo et al. (2021).

archival UV HST Space Telescope Imaging Spectrograph (STIS) E140M+E230M spectrum of this white dwarf (B. T. Gaensicke et al. 2015), which we retrieved from the HASP database (J. Debes et al. 2024), we find O, Si, Mg, and Fe absorption in the spectrum near the photospheric radial velocity (RV) of WD 0310–688 (see Figure 2). This suggests accretion of metal-rich material on the white dwarf, and we reclassify it as a DAZ. We also note the presence of the Si II 1265 Å line, indicating that the UV absorption lines are not from the interstellar medium (D. Koester et al. 2014) and confirming that there is pollution in the white dwarf's photosphere. Accretion has implications for the disk and exoplanet hypotheses, which we discuss more in Section 4, so we will further constrain this accretion here.

We construct a model of WD 0310–688 using an updated version of the model atmosphere code described by S. Blouin et al. (2018a, 2018b) and references therein. The model atmosphere code has been modified to include all relevant spectral lines and molecular bands up to 30 μm as described by M. A. Limbach et al. (2022).

We calculate $\log N({\rm Si})/N({\rm H}) = -8.1 \pm 0.2$ from the STIS spectrum by fitting three Si II lines (at 1260.42, 1264.73, and 1265.02 Å). For this white dwarf with a temperature of 15,865 K and $\log(g)$ of 8.076, the diffusion timescale of Si is 1.2×10^5 s (1.4 days; P. Dufour et al. 2017). The short diffusion timescales for this white dwarf are due to its high temperature, indicating that it must have been accreting in 2016 during the STIS observations. The thickness of the superficial convection zone is $10^{-16.6}$ of the total mass (P. Dufour et al. 2017). By dividing the mass of Si mixed in the convection zone by the sinking timescale, we obtain a steady-state accretion rate of Si of 5.3×10^4 g s^{-1}. Relative to Si, we find that the other metal abundances, listed in Table 2, are consistent with the bulk Earth (C. J. Allegre et al. 1995) once accounting for diffusion timescales. For Fe, the detection is marginal, so it is not given in the table, but if we assume a log Fe/Si that corresponds to bulk Earth, we get a synthetic spectrum consistent with the HST spectrum.

Assuming the accreted material has a bulk Earth composition and based on the steady-state accretion rate of Si, the total accretion rate is 3.3×10^5 g s^{-1}. This is among the lowest accretion rates observed in polluted white dwarfs (S. Blouin & S. Xu 2022). A summary of all the white dwarf's parameters from this work and the literature is provided in Table 2.

3.2. MEOW Data Analysis

3.2.1. Resolved Sources in the Image

Prior to conducting a detailed analysis, we visually inspected the color image for resolved sources that could be bound companions to the white dwarf. The purpose of this brief search is to note the presence of possible wide-orbit companions that could serve as perturbers (via planet–planet scattering; see Section 4), which is relevant to the IR excess detection presented within this Letter.

We identify several resolved sources in Figure 1 that exhibit colors and fluxes consistent with exoplanets. One of these is relatively close, about 80 au from the white dwarf. This source (which is not the primary focus of this Letter) is only detected with an SNR of a few but is consistent with a ∼140 K planet (which, given the system's age, would likely be sub-Jovian in mass; E. F. Linder et al. 2019). However, at this angular separation, the false-positive rate is reasonably high in our survey. There are also many other sources at larger angular separations from the white dwarf with photometry consistent with warmer, more massive exoplanet models. We expect that most or all of these point sources at large angular separations are background objects, but additional epochs of MIRI imaging could show whether any share common proper motion with the white dwarf, indicating that they are bound exoplanets. This information will be crucial for understanding exoplanet occurrence rates around white dwarfs and the systems' dynamical histories. However, we defer detailed consideration of the resolved point sources around WD 0310–688 until follow-up observations are conducted.

3.2.2. Photometry and IR Excess

In this subsection, we describe how we (1) reduce the data using a custom pipeline, (2) perform aperture photometry and report the measured flux values, (3) quantify the measurement errors, (4) compute the infrared excess from the photometry, and (5) provide checks to verify that the measured infrared excess is real and not attributable to any emission from the white dwarf itself.

Step 1: Data reduction—The MIRI imagery reduced automatically by the JWST pipeline and available in MAST suffers from a nonuniform flat-field subtraction at the reddest wavelengths. To address this, we reprocessed the data using a custom software package, `MEOW`, that is available on GitHub.[21] Version 1.0 of `MEOW` was used for this reduction. We used JWST pipeline version 1.15.1 and CRDS jwst _ 1225.pmap. The background-subtraction code is based on an STScI JWebbinar demo[22] that produces well-flat-fielded Stage 2 data with a custom background subtraction using the multiple dithers on each source.

Step 2: Aperture photometry—Using the reprocessed Stage 2 data, we then conducted aperture photometry on the white dwarfs in the MEOW data set. To conduct aperture photometry, we used the Python `photutils` package and the aperture correction values provided in the JWST CRDS[23] and color corrections table provided by the STScI HelpDesk.[24] For the aperture sizes, we used the values corresponding to the full array (as we read out the full MIRI subarray) and the 80% energy-encircled aperture sizes (the largest apertures with

---

[21] https://github.com/kevin218/MEOW

[22] https://github.com/spacetelescope/jwebbinar_prep/blob/jwebbinar31/jwebbinar31/miri/Pipeline_demo_subtract_imager_background-platform.ipynb

[23] https://jwst-crds.stsci.edu/; file version `jwst_miri_apcorr_0017.rmap`.

[24] https://stsci.box.com/shared/static/47xxtu2yq21tdfioey7q8dsd4ly8uwki.dat; `color_corrections_miri.dat`.

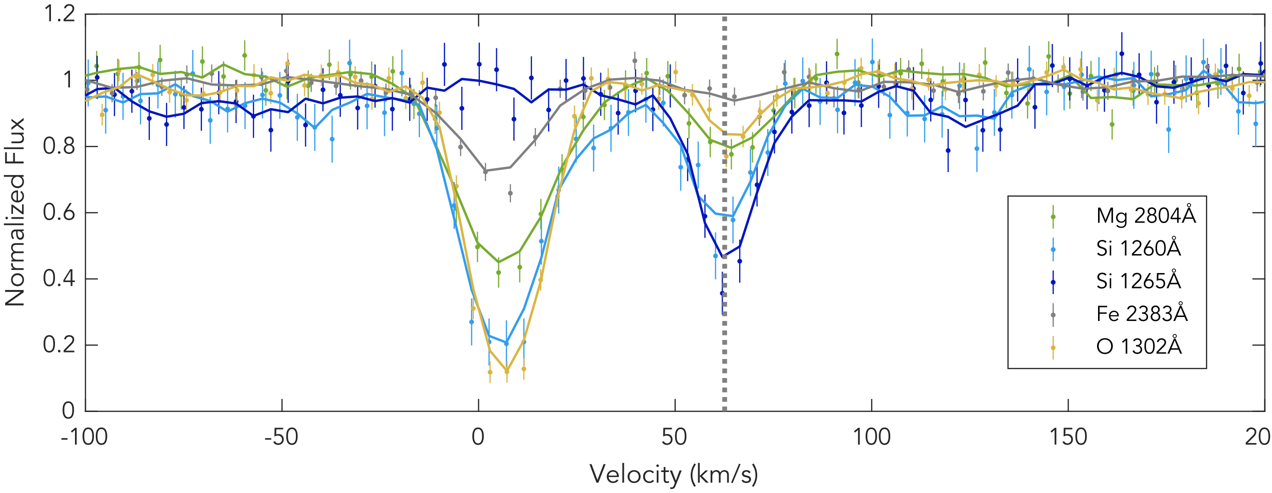

Figure 2. In a reanalysis of an archival HST/STIS spectrum of WD 0310–688, we detect atomic lines of four metals in the white dwarf's photosphere. This suggests accretion of metal-rich material onto the white dwarf, and we reclassify it as a DAZ due to the presence of the metal lines. WD 0310–688 previously was a DA spectral type.

Table 2
Summary of WD 0310–688 Parameters

Parameter	Value	References
Name	WD 0310–688	
Alt. name	CPD-69 177	
R.A. (ep = J2000)	03 10 31.0195960	(1)
decl. (ep = J2000)	−68 36 03.380768	(1)
R.A. proper motion (PM; mas yr^{-1})	39.668 ± 0.036	(1)
decl. PM (mas yr^{-1})	−103.237 ± 0.032	(1)
RV (km s^{-1})	62.6 ± 0.4	(2)
Parallaxes (mas)	96.1834 ± 0.0289	(1)
Distance (pc)	10.397 ± 0.003	(1)
Spectral type	DAZ	(3)
U (mag)	10.757	(5)
G (mag)	11.409583	(1)
K (mag)	11.861	(6)
T_{eff} (K)	15, 865 ± 263	(3), (4)
log g	8.076 ± 0.020	(3), (4)
Initial mass ($M_\odot$)	1.9 ± 0.4	(3), (4)
White dwarf mass ($M_\odot$)	0.659 ± 0.012	(3), (4)
Main-sequence lifetime (Gyr)	$1.4^{+1.4}_{-0.5}$	(3), (4)
White dwarf age (Gyr)	0.194 ± 0.013	(3), (4)
Total age (Gyr)	$1.6^{+1.4}_{-0.5}$	(3)
Accretion rate (g s^{-1})	3.3×10^5	(3)
log N(Si)/N(H)	−8.1 ± 0.2	(3)
log N(O)/N(H)	−7.2 ± 0.2	(3)
log N(Mg)/N(H)	−8.0 ± 0.2	(3)

References: (1) Gaia Collaboration 2020, (2) Napiwotzki et al. 2020, (3) this work, (4) Gentile-Fusillo et al. 2021, (5) Koen 2010, (6) Cutri 2003.

correction values available) on the target point-spread function (PSF).

The resulting measured flux values are given in Table 3. In each band, we measure the flux of the white dwarf at each of the four dithers separately and then report the white dwarf's median flux value, using the scatter in the flux measurements divided by the square root of the number of dithers to compute the error of the measured flux value.

Step 3: Error sources—The errors in the infrared excess measurement of white dwarfs in the MEOW sample arise from two primary sources: (1) the precision (signal-to-noise) of the measurement, which is primarily limited by photon noise (listed in the middle column in Table 3 for WD 0310–688), and (2) the accuracy with which our white dwarf models predict the star's flux. For the MEOW data, the limiting factor can either be photon noise or the accuracy of the JWST photometry and our models, depending on the bandpass and the brightness of the white dwarf. Notably, WD 0310–688, one of the brightest white dwarfs, is consistently limited by model/photometric accuracy across all bands.

Table 3
Measured White Dwarf Flux and IR Excesses

Band	Flux (μJy)	IR Excess (F_p/F_*) (%)
F770W	1063.5 ± 2.9	−0.9 ± 2
F1800W	230.4 ± 0.8	16.6 ± 2
F2100W	179.1 ± 0.7	21.3 ± 2

Step 4: Infrared excess—We compute the infrared excess, defined as the measured flux of the white dwarf relative to the expected (modeled) flux values. We build a model for each white dwarf using the same modeling process described in Section 3.1 for WD 0310–688. This analysis and IR excess calculation was conducted for all white dwarfs in the MEOW sample. Figure 3 illustrates the infrared excess (or deficit) divided by the precision of our measurement for a subset of the white dwarfs in the MEOW sample. Only white dwarfs without a large (>100 MG) magnetic field and those amenable to aperture photometry[25] are included in this plot. The white dwarfs included in the plot are WD 0839–327, WD 0840–136, WD 1309+853, WD 1820+609, WD 1756+827, WD 1019+637, WD 0752–676, WD 0821–669, and WD 0310–688. This measurement precision accounts for both error sources (1) and (2). In this plot, we take error (2) to be 2%, the absolute photometric precision of MIRI as discussed in Section 2.

In Figure 3, the green lines representing white dwarfs without notable IR excess are systematically low by 1%–2%. To address this, we apply a correction factor to the measured IR excesses where we have a sufficiently large set of white dwarfs

---

[25] For many MEOW targets, PSF fitting is necessary due to nearby sources contaminating the background.

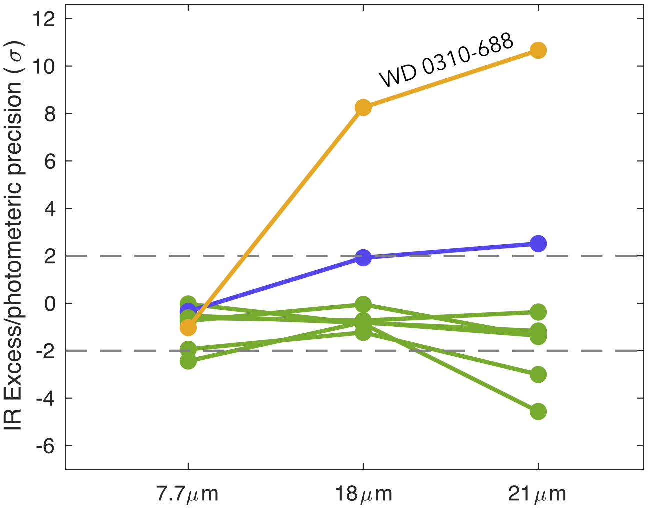

Figure 3. The measured IR excess or deficit divided by the precision of our measurement (y-axis) in all three spectral bands (x-axis) for a subset of MEOW white dwarfs. The orange line represents WD 0310–688, which shows a highly significant IR excess. The purple line corresponds to another white dwarf with an excess possibly due to an exoplanet but detected with less significance than WD 0310–688. The green lines indicate no significant excess, aligning generally with our models, although they are systematically low by 1%–2% at 7.7 μm and 21 μm. The white dwarf that is notably low at 21 μm is likely affected by a nearby bright red galaxy contaminating the background flux measurement.

with an SNR greater than 50 that can be used for calibration. At 7.7 μm, almost all white dwarfs meet this criterion, and at 18 μm, only a couple of the brightest white dwarfs in our sample do. The derived correction factors are 1.14% at 7.7 μm and 0.1% at 18 μm. At 21 μm, there are no comparatively bright white dwarfs that provide a good reference, so we do not apply an additional correction factor at 21 μm.

The IR excesses for WD 0310–688 (orange line), including the correction factors, are −0.9%, 16.6%, and 21.3% at the 7.7 μm, 18 μm, and 21 μm bands, respectively (as shown in Figure 4 and listed in Table 3). If the source of the excess is a planet, the infrared excess corresponds to the flux ratio of the planet to the star (F_p/F_*). We calculate the significance of the IR excess detected in the WD 0310–688 system to be 8.3σ at the 18 μm band and 10.7σ at the 21 μm band. No significant excess is detected at 7.7 μm.

The purple line in Figure 3 indicates a marginal detection of IR excess for WD 1309+853. This white dwarf has a relatively weak magnetic field of 5 MG, which could potentially account for the discrepancies between the photometry and the model. None of the other white dwarfs presented in this plot are known to have magnetic fields. A full analysis and discussion of the IR excesses within the MEOW sample is deferred to a later manuscript.

Step 5: Verifying the result—To further validate the robustness of the IR excess measurement for WD 0310–688, we conducted two additional tests. First, we compared the fluxes using the Stage 3 data available in MAST for our target, finding that the flux values agreed with our custom reduction results to within 2% in all bands (some deviation is expected due to a nonuniform flat field in the Stage 3 data).

Second, we generated a range of white dwarf models consistent with the $\pm 1\sigma$ uncertainties derived from the optical photometry and spectroscopy described in Section 3.1. Our analysis revealed that varying the white dwarf model does not produce an IR excess that increases with wavelength, as observed with MIRI. Instead, adjusting the white dwarf parameters results in a near-uniform shift in the IR excess across all MIRI wavelengths, owing to the fact that MIRI photometry samples the Rayleigh–Jeans tail of the white dwarf's spectral energy distribution (SED).

3.2.3. PSF Subtraction

In this section, we use PSF subtraction to constrain the maximum orbital separation of the IR excess source and determine the background source false-positive probability. In an attempt to directly image the source emitting the infrared excess, we conducted a PSF subtraction using our custom flat-field-corrected 21 μm Stage 2 data. We used four images of WD 0310–688 for the science frames (see Figure 5) and four reference images from the white dwarf WD 0839–327 ($G = 11.82$ mag), the white dwarf most similar to WD 0310–688 in our MEOW sample, as our reference PSF. We used the python package `VIP` (C. A. Gomez Gonzalez et al. 2017) to crop the images to a size of 100 pixels (1″), correct NaN values, and align the PSFs to a common center. We then scaled the reference PSF to the science PSF and performed a PSF subtraction (results are shown in Figure 5, center column). We find no notable residuals in the subtraction, suggesting that the source of infrared excess is unresolved from the star.

We then injected companions with the same flux as the detected IR excess at various separations from the target. We find we are able to detect the injected companions after PSF subtraction with a confidence of $>4\sigma$ when the companion is injected at separations of >2 au; therefore, we constrain the source to be within 2 au of the host.

The PSF subtraction constrains the maximum separation of the infrared excess source to <2 au, or $<0\farcs19$. Using this maximum separation, we calculated the probability that our infrared excess is due to a background object rather than something in the WD 0310–688 system. The MIRI field of view is $112\farcs6 \times 73\farcs5$, which corresponds to a false-positive rate of 1/73,000 if there was one false positive in the field of view and we observed only one white dwarf. However, MEOW images typically contain four sources within the field of view that are consistent with exoplanet SEDs, and the MEOW survey has observed 17 targets. Assuming the four planetlike sources per field are false positives (though some may actually be planets), we estimate the probability that the IR excess we have detected is a background source to be 1/73,000 times 4 false positives/field and 17 targets, giving a false-positive probability of <0.1%. We note that none of the MEOW targets with reliable photometry (no contamination from nearby sources) exhibit an IR excess, except for those with known magnetic fields. We also note that the WD 0310–688 field is less dense than most of the others within the MEOW survey, making this estimate likely conservative. Due to the very low false-positive probability, we conclude that the IR excess is almost certainly associated with the white dwarf system.

3.2.4. Blackbody Retrieval

Having ruled out background sources as a plausible explanation for the infrared excess, we conclude that the IR excesses are likely due to a cold dust disk or an exoplanet. We now explore models that can explain the measured excess.

Because we only have three photometric data points, the data do not justify a model more complex than a blackbody. The

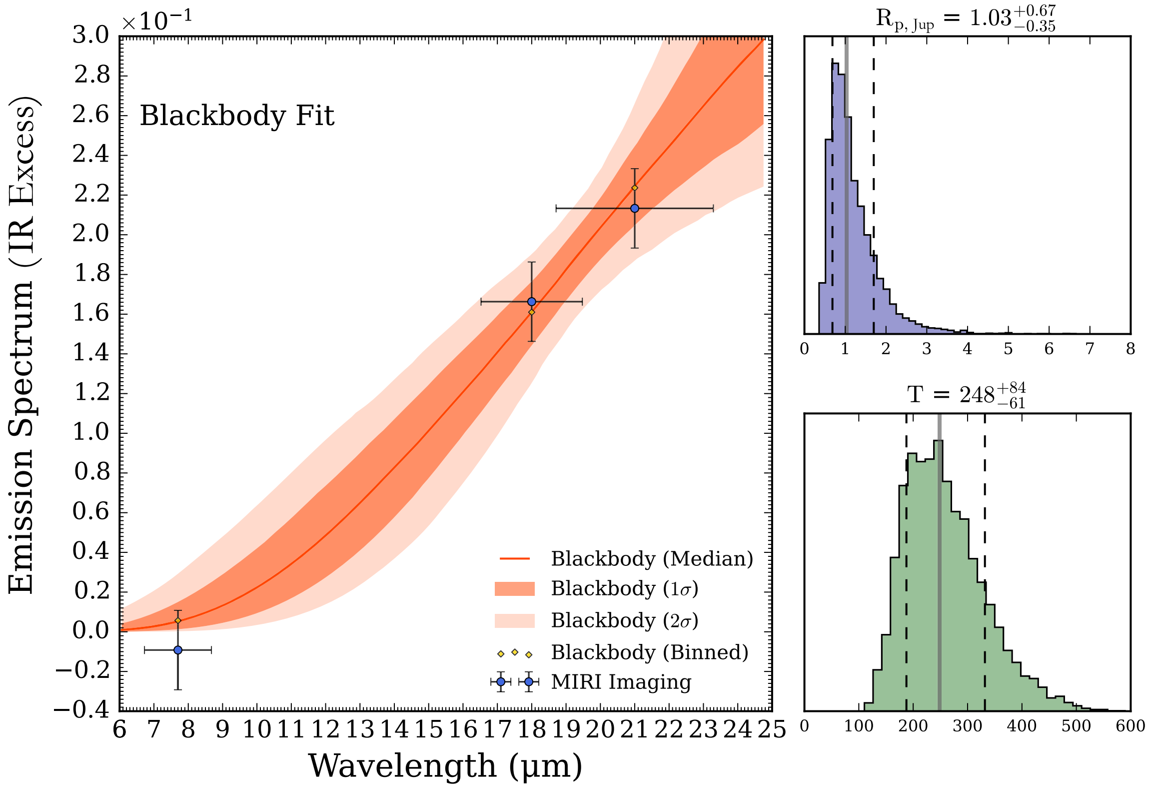

Figure 4. Measured wavelength-dependent infrared excess (i.e., the planet-to-star flux ratio, if the source of the infrared excess is a planet) from three photometric bands collected with JWST MIRI (F770W, F1800W, and F2100W). The infrared excess is consistent with a blackbody of temperature 248^{+84}_{-61} K and an emitting area of $1.03^{+0.67}_{-0.35}$ R_{Jup}. Using the derived system age, the planet's temperature, and planet cooling curves, we estimate a planet mass of $3.0^{+5.5}_{-1.9}$ M_{Jup}.

advantage of a blackbody model is that it is agnostic as to whether the source is a disk or an exoplanet, as both are, to first order, blackbodies in the mid-infrared.

We conducted a blackbody fit using the measured infrared excess. In Figure 4, we plot the measured excess alongside the temperature and size constraints from our blackbody fit. The fit to the photometric measurements yields a $T = 248^{+84}_{-61}$ K blackbody with an emitting area of $1.03^{+0.67}_{-0.35}$ R_{Jup}.

We note that the size of the emitting body is conspicuously close to that of a giant planet, but we do not disregard the possibility that a cold dust disk could also have an emitting area coincidentally similar to that of a gas giant planet. However, this would constitute a very unusual cold dust disk, as discussed in Section 4. We attempted to run more complex atmospheric retrievals on the data but found that this resulted in no additional meaningful constraints on the source.

3.2.5. Minimum Orbital Separation

We calculate the minimum orbital separation, a, of the source using the fitted blackbody temperature as the equilibrium temperature, T_{eq}. This calculation assumes that the measured brightness temperature is equal to the blackbody temperature, which is a reasonable assumption in the mid-infrared, and that there is perfect heat redistribution. The orbital separation is given by

$$a = R_{*}(1 - \alpha)^{\frac{1}{2}}\left(\frac{T_{\mathrm{eff}}}{T_{\mathrm{eq}}}\right)^{2}, \quad (1)$$

where R_* is the radius of the star, α is the albedo of the planet, and T_{eff} is the effective temperature of the white dwarf. This results in a minimum orbital separation of $0.18^{+0.14}_{-0.08}$ au (with $\alpha = 0.4$; a typical infrared albedo for a highly reflective gas giant). The 1σ lower bound gives a minimum orbital separation of 0.10 au. Orbital separations <0.1 au would result in higher brightness temperatures that are inconsistent with the fit. This constraint assumes a circular orbit. However, if the planet has a highly eccentric orbit (and is migrating), it may pass much closer to the white dwarf, becoming significantly hotter during parts of its orbit. If the source is a optically thin disk (e.g., zodi-like) rather than a planet, the same orbital constraint ($0.18^{+0.14}_{-0.08}$ au) holds. The exception would be if the source is a planet and exhibits an exceptionally high albedo (e.g., $\alpha > 0.4$), which could potentially allow for slightly closer separations.

3.2.6. Mass Estimation

If the source is an exoplanet, we can derive a mass estimate using exoplanet evolutionary models. Using the age of the system and the planet's temperature, along with the 1σ uncertainties in these two parameters, we constrain the planet's mass to $3.0^{+5.5}_{-1.9}$ M_{Jup} (M. S. Marley et al. 2021), assuming no heat comes from irradiation. If the planet is out at 1–2 au, the stellar irradiation has essentially no effect on the inferred mass because it would be dominated by the internal heat of the planet, so at those distances, the evolutionary masses apply, as previous studies suggest that modest irradiation does not change the cooling very much (J. J. Fortney et al. 2007).

However, at closer separations, irradiation from the white dwarf could change the evolutionary inferred mass. If the planet orbits close to the white dwarf (∼0.1 au), its flux must be dominated by reradiated stellar radiation. In this scenario, the mass could be much lower. We can still place a lower limit

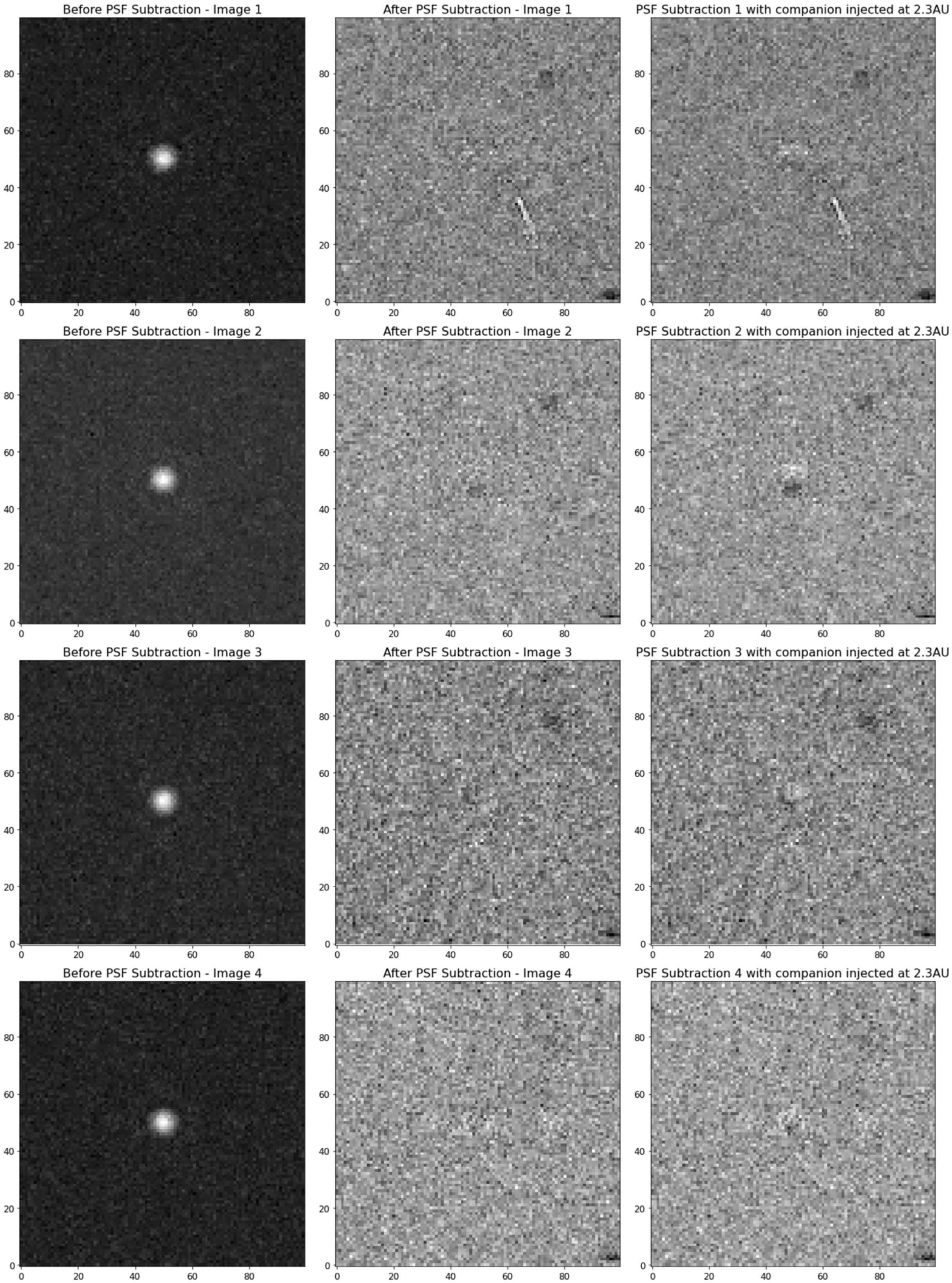

Figure 5. Left: WD 0310–688 at 21 μm in each of the four dithers. Center: PSF subtraction at each of the four dithers. Note that the cosmic ray in the first dither and the negative source at a $\sim$30 pixel separation is in the reference star image, not the science image. Right: PSF subtraction after a companion that is 21% of the brightness of the star was injected at 2.3 au. This injected source is retrieved with a statistical significance of 7.0σ (at each dither, the significance of the detections are 3.2σ, 4.2σ, 3.7σ, and 2.7σ). Injected sources are successfully retrieved at $>4\sigma$ when injected at separations of >2 au; therefore, we constrain the detected IR excess source to be within 2 au of the host.

on the mass based on the fact that we need the planet to be sufficiently large in radius. We estimate the minimum mass based on the minimum planet radius from our blackbody fit within the 1σ constraint, which is $0.68\,R_{\rm Jup}$. Using the E. F. Linder et al. (2019) models, at an age of 1.1 Gyr, we estimate a minimum mass of $0.2\,M_{\rm Jup}$ (slightly less massive than Saturn). However, we note that empirically, there are Jupiter-sized objects with masses as low as a few Earth masses, such as the Kepler 51 superpuffs (K. Masuda 2014; J. E. Libby-Roberts et al. 2020).

3.3. Other Constraints on Companions

3.3.1. Astrometry

If WD 0310–688 is indeed orbited by a giant planet, we can place further constraints on its properties using astrometry. The most precise existing astrometric observations for this target are from the Gaia mission (Gaia Collaboration et al. 2016); however, the Gaia epoch astrometry is not yet available, precluding any straightforward search for companions. Nevertheless, it is possible to extract some limits on companion properties from the published Gaia DR3 astrometric solution.

The Gaia renormalized unit weight error (RUWE) parameterizes the significance excess noise of the astrometric data. Conventionally, an RUWE above >1.4 is interpreted as significant evidence in favor of astrometric variability (L. Lindegren 2018). In Gaia DR3, WD 0310–688 has an RUWE of only 1.13, which suggests that there is no strong evidence for orbital motion in the underlying epoch astrometry.

We then attempt to convert the RUWE into a set of upper limits on companion masses. We follow the method of V. Belokurov et al. (2020) and V. Korol et al. (2022) to invert the RUWE into the normalized astrometric perturbation, $\delta\theta$. As the observed RUWE is not significant, we employ RUWE < 1.4 as a conservative limit on the astrometric noise, which then gives an assumed limit of $\delta\theta < 0.19$ mas. For orbital periods shorter than or approximately equal to the 1038 day observational baseline of Gaia DR3 (L. Lindegren et al. 2021), we can assume that this approximates the rms of the astrometric reflex amplitude of the theorized orbit. This allows us to assume the conventional astrometric amplitude relation,

$$\alpha = \frac{m}{M_*}\frac{a}{D}, \tag{2}$$

where α is the astrometric amplitude in arcseconds, m is the companion mass, M_* is the stellar mass, a is the semimajor axis in au, and D is the distance in parsecs (A. Sozzetti 2005). As M_* and D are known for WD 0310–688, we can derive an upper limit on allowed companion masses as a function of semimajor axis within $\lesssim$2 au.

More stringent constraints can be made on companions with wider orbits using Hipparcos–Gaia astrometry (T. D. Brandt 2018; P. Kervella et al. 2019). WD 0310–688 was one of only 20 white dwarfs bright enough to be successfully observed with Hipparcos (HIP 14754; G. Vauclair et al. 1997), and when combined with the more recent Gaia astrometry, the 25 yr time baseline allows for strong constraints on longer-period planets. In the Hipparcos–Gaia Catalog of Accelerations (T. D. Brandt 2021), there is no significant evidence for an astrometric acceleration; the difference between the Gaia proper motion and the averaged Hipparcos–Gaia proper motion in R.A. and decl. is $\Delta\mu = (-0.017 \pm 0.075,\ -0.012 \pm 0.080\ {\rm mas\ yr}^{-1})$, respectively, equivalent to $\Delta v = (-0.8 \pm 3.7,\ -0.6 \pm\ 3.9\ {\rm m\ s}^{-1})$ in physical units (A. Venner et al. 2021, Equations (9) and (10)). We can thus set a strict 3σ upper limit of $<11\ {\rm m\ s}^{-1}$ on the Hipparcos–Gaia tangential velocity anomaly.

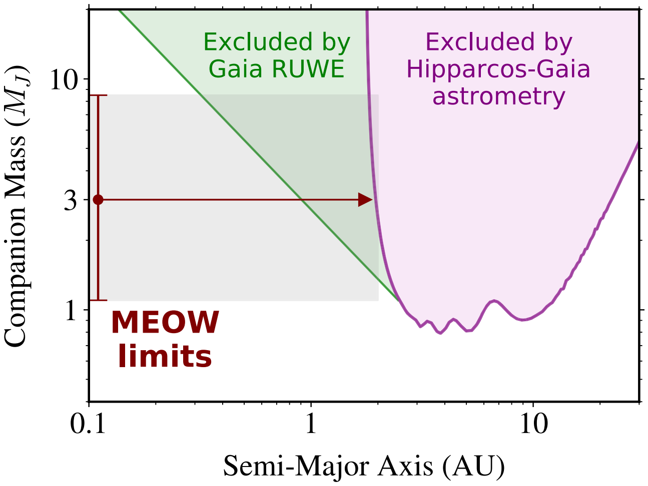

Figure 6. Constraints on the planets orbiting WD 0310–688 from astrometry. We overplot the planetary parameters implied by the infrared excess, assuming that the upper limit in projected separation translates to semimajor axis. The absence of a large Gaia DR3 RUWE helps to exclude the more distant, massive edge of the parameter space, but within $a < 1$ au, the sensitivity of astrometry is low. At larger distances (2.5–10 au), planets with masses as low as $1\,M_{\rm Jup}$ can be ruled ruled out due to the absence of a significant Hipparcos–Gaia acceleration.

We plot the constraints on companion mass as a function of semimajor axis afforded by the astrometric nondetections in Figure 6. Between ≈1 and 2 au, the low RUWE allows us to exclude planets more massive than $\gtrsim 3\,M_{\rm Jup}$. For wider separations, we use the method of P. Kervella et al. (2019) to calculate mass limits from the Hipparcos–Gaia astrometry, from which we find that planets with masses as low as $1\,M_{\rm Jup}$ can be excluded between 2.5 and 10 au. These constraints agree well with and marginally improve upon the nondetection of planets at projected separations above >2 au in the MIRI imaging. However, we cannot independently confirm or reject close-separation planets with the existing astrometric data. Our existing astrometric constraints have low sensitivity to planetary-mass companions within $a < 1$ au.

If the MIRI infrared excess is indeed caused by a giant planet within 2 au of WD 0310–688, it may be possible to detect the reflex orbital motion in the epoch astrometry that will be released in Gaia DR4. H. Sanderson et al. (2022) predict that Gaia astrometry will lead to the detection of 8 ± 2 giant planets around white dwarfs; however, they have assumed that essentially none of these planets will be found within <2 au as a result of destruction during stellar evolution.

3.3.2. Doppler Monitoring

In 2023 December, we observed WD 0310–688 using the Magellan Carnegie Planet Finder Spectrograph (PFS; J. D. Crane et al. 2006, 2008, 2010) to attempt Doppler monitoring for the planet candidate. Although WD 0310–688 is metal-polluted, only the hydrogen Balmer lines were detectable in the PFS spectrum due to the low level of pollution. Using these lines, we achieved a precision of about $400\ {\rm m\ s}^{-1}$ over 15 minutes, or $200\ {\rm m\ s}^{-1}\ {\rm night}^{-1}$ with 1 hr monitoring. If orbiting at the minimum separation of 0.1 au, the planet must have a mass near or below the lower end of the self-luminous mass range (e.g., $<1.1\ M_{\rm Jup}$, as determined in Section 3.2.6), or it would be hotter than 248 K. At this separation and mass, we would expect an RV semiamplitude of $120\ {\rm m\ s^{-1}}$. Based on this initial observation, we conclude that detecting the planet via RV monitoring would require an intensive observation program, even if the planet is located in the most favorable part of the allowed parameter space. For the majority of the parameter space, this method is not feasible. Therefore, Doppler monitoring is not a practical method for confirming this planet. However, RV confirmation may be feasible for white dwarf planet candidates with more metal lines in the visible spectrum or with shorter orbital periods (L. K. Rogers et al. 2024).

3.3.3. Other Mid-IR Photometry

We searched for archival data that could aid in illuminating the source of the infrared excess. We find that archival Spitzer data show no detectable IR excess. The absence of a Spitzer 8 μm (IRAC band 4) detection of infrared excess (F. Mullally et al. 2007) is consistent with our nondetection of IR excess in the MIRI 7.7 μm band. In the Wide-field Infrared Survey Explorer (WISE) band 3 (12 μm), we measure an IR excess of $16\% \pm 14\%$. Although this excess is consistent with our MIRI detection, it is also consistent with no excess at 1.1σ, so it provides little additional constraint on the system. In the WISE band 4 observations, the archival measurements do not provide sufficient sensitivity to produce any meaningful constraint on this source.

4. Discussion

We have detected infrared excess emission toward WD 0310–688, and we have shown that the emission is almost certainly coming from the white dwarf system. We can identify two likely explanations: a giant planet or a cold debris disk. Here, we consider the two hypotheses, give arguments in each of their favor, and discuss the implications of each being correct.

4.1. Giant Planet

The first option we consider is a giant planet. It would have a radius similar to that of Jupiter, a mass of $3.0^{+5.5}_{-1.9}\ M_{\rm Jup}$, and an orbital separation between 0.1 and 2 au. The arguments in favor of this hypothesis are as follows.

1. Planets of this mass are expected to exist around white dwarfs if they survive the star's red giant phase, particularly since A-type stars have higher rates of giant planet occurrence (S. Reffert et al. 2015).
2. A wide range of objects, from gas giant planets as small as Saturn to late M dwarfs, have emitting areas similar to Jupiter, whereas debris disks can vary greatly in size. The radius inferred from a blackbody fit corresponds to the emitting area of a gas giant, which is suggestive.

The arguments against this hypothesis are as follows.

1. The emitting source is close to the white dwarf, which is expected to be rare. We know giant planets orbiting main-sequence stars that are close enough to transit are rare (L. van Sluijs & V. Van Eylen 2018; A. Robert et al. 2024). Given our small sample size, one detection does not necessarily indicate a common phenomenon, but finding something so unusual so quickly is surprising. Nevertheless, the short-period giant planet WD 1856b exists (A. Vanderburg et al. 2020), and this planet candidate could be a younger analog of that system's planet. Exoplanet astronomy has a history of discovering rare objects sooner than their actual occurrence rates would suggest (B. T. Gansicke et al. 2006; D. Charbonneau et al. 2009; A. Vanderburg et al. 2015; M. Gillon et al. 2016).
2. Modeling the star's evolution (see the Appendix) suggests that the planet is orbiting in a forbidden location (J. Nordhaus & D. S. Spiegel 2013), making it difficult to explain its existence. One explanation that has previously been invoked to explain short- and intermediate-period orbits around white dwarfs is common envelope evolution, in particular, scenarios involving additional energy sources beyond the planet's gravitational energy (L. Chamandy et al. 2021; F. Lagos et al. 2021; A. Merlov et al. 2021) or scenarios where the planet is engulfed at the end of the asymptotic giant branch phase, and mass loss facilitates the ejection of the envelope (N. Yamaguchi et al. 2024). However, we argue that a common envelope scenario is unlikely to be a good explanation for an intermediate-separation planet around WD 0310–688. It is already energetically difficult to make common envelope evolution work for WD 1856b. For this planet, which is at a much wider orbital separation than WD 1856b, this explanation would be even more challenging because the amount of orbital energy available to eject the envelope is significantly less. Even greater amounts of additional energy would be required to prevent the planet from crashing into the core (L. Chamandy et al. 2021; F. Lagos et al. 2021; A. Merlov et al. 2021). An alternative explanation for the presence of an intermediate-period planet around WD 0310–688 is that the planet is currently undergoing tidal migration. However, in order for tidal migration to take place, the planet's eccentricity must be excited to very high values by additional massive objects in the system. There are no binary companions to this star that could drive tidal migration; however, we observe numerous planet candidates at or beyond 80 au distant in the MEOW images of WD 0310–688. Despite a high contamination rate from background active galactic nuclei in our survey, if one of these sources is indeed a planet bound to the white dwarf, it could plausibly serve as a Kozai perturber, where the distant companion induces oscillations in the inclination and eccentricity of a planet's orbit, potentially leading to high eccentricity and subsequent tidal migration (D. J. Munoz & C. Petrovich 2020; A. P. Stephan et al. 2021). Planet–planet scattering is another plausible mechanism that could be responsible for the planet's current position (J. H. Debes et al. 2012; D. Veras et al. 2016; R. F. Maldonado et al. 2021, 2022). Although close-in companions (<80 au) are absent, it is also plausible that an object may have been ejected from this system after interacting with our planet candidate.

4.2. Debris Disk

Another possibility we consider is a disk. Converting an IR excess into precise debris disk parameters is challenging, but we can approach this in a couple of ways. First, we can assume that

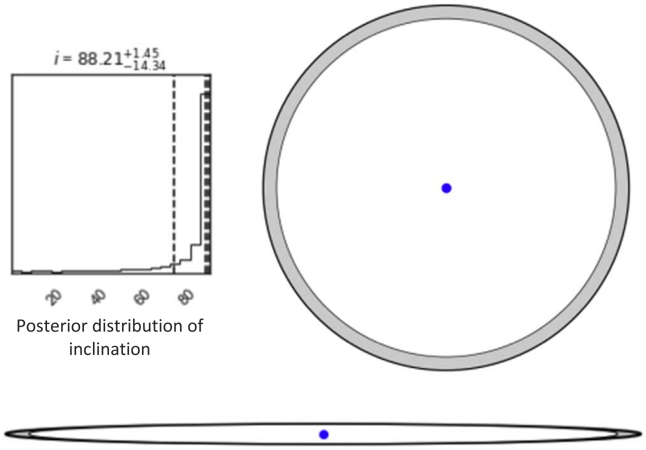

Figure 7. Posterior of the disk inclination from the Jura disk model fit (upper left) and a schematic of the disk viewed at 88°21 (bottom) and face-on (upper right) for comparison.

the disk is optically thin and/or puffed up, similar to exozodiacal light. Under this assumption, and using the temperature of 248 K from our blackbody fit for the dust, the semimajor axis would be 0.11 au, assuming an albedo of $\alpha = 0.06$, similar to that of interplanetary dust in our solar system (H. Yang & M. Ishiguro 2015). The effective emitting area of the disk would be approximately the same as the surface area of Jupiter.

Alternatively, we can assume an optically thick, thin, flat disk (M. Jura 2003). Using Markov Chain Monte Carlo to fit the IR excess with the Jura disk model, we obtained the following parameters. In this case, the disk is a very skinny ring with an inner radius of 171 $R_{\rm WD}$ and outer radius of 185 $R_{\rm WD}$ and is inclined nearly edge-on (see Figure 7).

The arguments in favor of this hypothesis are as follows.

1. Dust disks are common around white dwarfs, and although we have not previously observed one at such a cold temperature (J. Farihi et al. 2010), this is likely due to the lack of sensitivity before the advent of JWST. It is often more likely to encounter an unusual manifestation of a common phenomenon, like a debris disk, than a typical presentation of an uncommon phenomenon, such as a planet in an unlikely orbital configuration forbidden zone. This aligns with the principle of considering the most probable explanations before exploring less likely alternatives.
2. The white dwarf is polluted, as discussed in Section 3.1.2, and a debris disk is the most probable source of the pollution (although we note that pollution does not preclude the presence of close-in planets; B. T. Gänsicke et al. 2019). Infrared observations indicate that white dwarfs with observed debris disks are heavily polluted, typically with a total accretion rate $>3 \times 10^8$ g s^{-1} (J. Farihi et al. 2009), much higher than the accretion rate we measure for WD 0310–688.

The arguments against this hypothesis are as follows.

1. In order to explain the IR emission with a disk model, we must finely tune the disk's geometry to give a surface area similar to Jupiter. In particular, the best-fit parameters for an optically thick disk seem a bit contrived, with an extremely thin ring (only 7% of the disk's radial extent) and a nearly edge-on inclination. However, other disks have been found with similarly thin ring geometries (N. P. Ballering et al. 2022), and there is no reason that such disks could not be precisely aligned with our line of sight, so such a seemingly unusual geometry cannot be ruled out.
2. The location of the dust in the optically thin case is well outside the Roche limit, which would be contrary to our normal picture of white dwarf disks and pollution (although see the discovery of transiting systems outside the Roche radius for the rocky material that typically makes up dusty debris disks; Z. Vanderbosch et al. 2020; J. Farihi et al. 2022).

4.3. *Implications of the Discovery*

Regardless of the underlying cause, this IR excess is expanding our understanding of white dwarf planetary systems.

4.3.1. *If It Is a Planet*

Confirming this source as an exoplanet would be particularly exciting for several reasons. It represents the closest planet candidate around a white dwarf discovered to date, at a distance of 10.4 pc. It is the first planet candidate identified using the infrared excess detection technique. It is the first white dwarf planet candidate discovered at an intermediate separation (0.1–2 au). If confirmed, it would be one of the coldest worlds for which direct spectral atmospheric characterization is possible.

Furthermore, the host is a remnant of an A or late B star, and the planet would offer critical demographic constraints on this population, which is challenging to study by other means. With few exceptions, planets around A- and B-type main-sequence stars are generally accessible only through high-contrast imaging. Searches for such planets have yielded several detections (e.g., A.-M. Lagrange et al. 2010; M. Janson et al. 2021a) but are typically limited to planets at relatively large semimajor axes (tens or hundreds of au; E. L. Nielsen et al. 2019; M. Janson et al. 2021b; A. Vigan et al. 2021). Past the main sequence, in the red giant phase, the stars have expanded and cooled sufficiently to be more suitable for RV studies. Such studies have also yielded several planet candidates in the relevant stellar mass range (e.g., J. A. Johnson et al. 2007; S. Reffert et al. 2015), though in this case the detection range is limited to small separations in the range of typically a few au, and the actual estimation of stellar mass is subject to large uncertainties (e.g., J. P. Lloyd 2011; J. A. Johnson et al. 2013). As we have seen above, white dwarf imaging with JWST can cover planets over the whole separation space from the Roche limit (via infrared excess) up to hundreds of au (via resolved imaging) simultaneously, providing a much more complete demographic overview for the stellar remnant phase of massive stars. Comparisons with the main-sequence and red giant demographics can also provide the first constraints on how planetary systems are affected through the late stages of stellar evolution.

4.3.2. *If It Is a Disk*

Only three white dwarf disks have previous Spitzer/MIPS measurements: G29–38 (W. T. Reach et al. 2005), GD 56, and GD 133 (M. Jura et al. 2007). Few distant and cold disk candidates have been identified around hot, bright white dwarfs with Spitzer at 24 μm. A notable instance is the central star of the Helix Nebula (K. Y. L. Su et al. 2007). However, their interpretation as cold dust disks is complicated by dusty outflows associated with their immediate progenitors and binarity (Y.-H. Chu et al. 2011; G. C. Clayton et al. 2014). If this source is actually a disk rather than a planet, it would be perhaps unusual compared with other known white dwarf disks and could significantly expand our understanding of how planetary debris is accreted onto polluted white dwarf stars (C. H. Chen et al. 2020).

If confirmed as a debris disk, this system, alongside PG 1225–079 (J. Farihi et al. 2010), would represent one of the coldest debris disks ever detected around a white dwarf. These disks may signify distinct evolutionary stages—either at the nascent phase, where the disk is just beginning to form, or nearing the terminal phase, where the disk is predominantly dissipated. A. Bonsor et al. (2017) predicted that JWST would uncover numerous small debris disks, suggesting that such findings may be more common than previously anticipated.

Finally, considering our estimated accretion rate, if this source is indeed a debris disk, it would represent the white dwarf system with the lowest known accretion rate associated with a detectable disk.

4.4. How to Distinguish the Two Scenarios

The existing data on this system do not provide enough information to definitely differentiate between the planet and disk hypotheses. We surmise that the easiest way to differentiate between the two will be to obtain a MIRI medium-resolution spectrometer (MRS) spectrum of the blended SED. Even in the case of a cloudy planet, several hours of MRS time enables the detection of atmospheric features in an exoplanet's atmosphere that would provide concrete evidence of a planet. Conversely, a lack of detection of planetary atmospheric features consistent with an exoplanet atmosphere would provide strong evidence that the source of infrared excess is instead a cold dust disk. If it is indeed a debris disk, very likely it will have a 10 μm silicate feature, which has been seen in white dwarf disks with mid-infrared data (M. Jura et al. 2009; A. Swan et al. 2024).

5. Conclusions

In this Letter, we described the detection of infrared excess around the white dwarf WD 0310–688 and found the following.

1. The IR excess is best fit by a blackbody with a temperature of 248^{+84}_{-61} K and an emitting area of $1.03^{+0.67}_{-0.35}$ $R_{\rm Jup}$.
2. The source of the IR excess is constrained to be within 0.1–2 au, corresponding to orbital periods of 14 days to 3.4 yr.
3. If the emitting source is an exoplanet, its mass is constrained to $3.0^{+5.5}_{-1.9}$ $M_{\rm Jup}$, though it could be as low as 0.2 $M_{\rm Jup}$ if the planet's heat comes from irradiation.

The detection of a source, whether it is a planet or a cold dust disk, at this separation is unprecedented. It is one of only a handful of known white dwarf planets or planet candidates. It represents the nearest planet candidate around a white dwarf discovered to date, at a distance of 10.4 pc. It is the first planet candidate ever identified using the infrared excess detection technique. This technique is well suited for the detection of white dwarf exoplanets and may reveal many more candidates during JWST's lifetime.

It is the first white dwarf planet candidate discovered at an intermediate separation (0.1–2 au). This is particularly significant because planets at this separation are expected to have been destroyed during the star's red giant phase. Therefore, if confirmed, the planet must have migrated to its current location after the star evolved into a white dwarf. Confirming and further study of this planet will be crucial for understanding post-main-sequence planetary evolution and the fate of planets as their host stars die.

We determine that follow-up observations with JWST MRS will enable us to confirm the source of the IR excess as a planet and rule out the disk hypotheses. If confirmed, it will be one of the coldest worlds for which direct spectral atmospheric characterization is possible. Subsequent spectroscopic observations could allow for comparative studies with the coldest directly imaged free-floating planetary-mass worlds (such as the mid-Y dwarf WISE 0855–0714, which is comparable in mass, age, and temperature; K. L. Luhman et al. 2024).

Acknowledgments

The authors thank an anonymous reviewer for a thorough and helpful review of this Letter. We would like to thank Misty Cracraft, Karl Gordon, and the JWST Helpdesk for support with MIRI calibration files and absolute flux calibrations. This research has made use of the SIMBAD database, operated at CDS, Strasbourg, France (M. Wenger et al. 2000). This research has made use of the NASA Exoplanet Archive, which is operated by the California Institute of Technology, under contract with the National Aeronautics and Space Administration under the Exoplanet Exploration Program. This Letter leverages data gathered with the 6.5 m Magellan Telescopes located at Las Campanas Observatory, Chile. This work is based (in part) on observations made with the NASA/ESA/CSA James Webb Space Telescope. The data were obtained from the Mikulski Archive for Space Telescopes at the Space Telescope Science Institute, which is operated by the Association of Universities for Research in Astronomy, Inc., under NASA contract NAS 5-03127 for JWST. These observations are associated with program No. 4403. Support for program No. 4403 was provided by NASA through a grant from the Space Telescope Science Institute, which is operated by the Association of Universities for Research in Astronomy, Inc., under NASA contract NAS 5-03127.

Facilities: JWST, HST, Gaia, Hipparcos, Magellan, Spitzer, WISE. All the JWST data used in this Letter can be found in MAST: doi:10.17909/cjkx-kp07.

Software: `astro.py` (Astropy Collaboration et al. 2013, 2018, 2022), `numpy.py` (S. van der Walt et al. 2011), `wdwarfdate` (R. Kiman et al. 2022), `POSEIDON` (R. J. MacDonald & N. Madhusudhan 2017; R. J. MacDonald 2023), `MESA` version v7503 (B. Paxton et al. 2011, 2013, 2015; A. Dotter 2016; J. Choi et al. 2016), `SAOImage DS9` (Smithsonian Astrophysical Observatory 2000), `VIP` (C. A. Gomez Gonzalez et al. 2017), `corner.py` (D. Foreman-Mackey 2016). `ChatGPT` was utilized to improve wording at the sentence level and assist with coding inquires. Last accessed in 2024 August.

Appendix
The Implications of Stellar Evolution on a Planet's Orbit

We can draw insights as to whether the planetary companion falls into the forbidden zone by investigating the current orbital

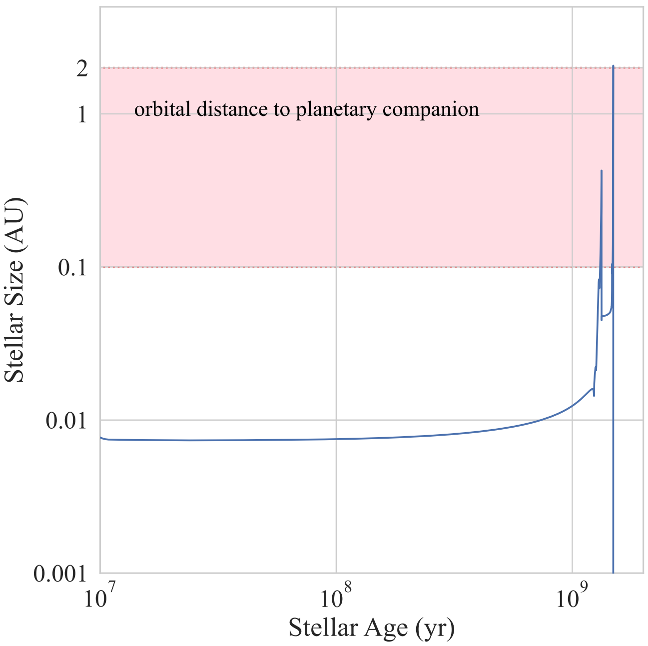

Figure 8. Evolution of the stellar radius as a function of age for a 1.9 $M_\odot$ star, simulated using `MESA` Isochrones & Stellar Tracks (`MESA` version v7503). The pink shaded region represents the range of possible orbital separations of the planetary companion (0.1–2 au). The dotted lines mark the bounds of this range. The maximum radius reached by the star at the tip of the RGB (2.1 au) exceeds even the most generous estimate of the orbital separation, indicating that the planetary companion likely falls into the forbidden zone.

separation in comparison to the size of the host when it was at the tip of the red giant branch (RGB). To this end, we simulated the evolution of a 1.9 $M_\odot$ star using `MESA` Isochrones & Stellar Tracks[26] (`MESA` version v7503; B. Paxton et al. 2011, 2013, 2015; J. Choi et al. 2016; A. Dotter 2016). We investigated a range of initial metallicities, determining that the orbital separation of the planet was within the maximum RGB radius in all cases. In Figure 8, we illustrate the change in stellar size as a function of age. The estimated bounds of the orbital separation of the companion, 0.1–2 au, are shown as dotted lines, and the intermediary range between these extremes is highlighted in pink. Note that even the most generous orbital separation estimate is less than the maximum RGB size of the host (2.1 au).

ORCID iDs

Mary Anne Limbach https://orcid.org/0000-0002-9521-9798
Andrew Vanderburg https://orcid.org/0000-0001-7246-5438
Alexander Venner https://orcid.org/0000-0002-8400-1646
Simon Blouin https://orcid.org/0000-0002-9632-1436
Kevin B. Stevenson https://orcid.org/0000-0002-7352-7941
Ryan J. MacDonald https://orcid.org/0000-0003-4816-3469
Sydney Jenkins https://orcid.org/0000-0001-9827-1463
Rachel Bowens-Rubin https://orcid.org/0000-0001-5831-9530
Melinda Soares-Furtado https://orcid.org/0000-0001-7493-7419
Caroline Morley https://orcid.org/0000-0002-4404-0456
Markus Janson https://orcid.org/0000-0001-8345-593X
John Debes https://orcid.org/0000-0002-1783-8817
Siyi Xu https://orcid.org/0000-0002-8808-4282
Evangelia Kleisioti https://orcid.org/0009-0004-8080-5358
Matthew Kenworthy https://orcid.org/0000-0002-7064-8270
Paul Butler https://orcid.org/0000-0003-1305-3761
Jeffrey D. Crane https://orcid.org/0000-0002-5226-787X
Dave Osip https://orcid.org/0000-0003-0412-9664
Stephen Shectman https://orcid.org/0000-0002-8681-6136
Johanna Teske https://orcid.org/0009-0008-2801-5040

References

Agol, E. 2011, ApJL, 731, L31
Alcock, C., Fristrom, C. C., & Siegelman, R. 1986, ApJ, 302, 462
Allegre, C. J., Poirier, J.-P., Humler, E., & Hofmann, A. W. 1995, E&PSL, 134, 515
Astropy Collaboration, Price-Whelan, A. M., Lim, P. L., et al. 2022, ApJ, 935, 167
Astropy Collaboration, Price-Whelan, A. M., Sipőcz, B. M., et al. 2018, AJ, 156, 123
Astropy Collaboration, Robitaille, T. P., Tollerud, E. J., et al. 2013, A&A, 558, A33
Ballering, N. P., Levens, C. I., Su, K. Y. L., & Cleeves, L. I. 2022, ApJ, 939, 108
Barber, S. D., Patterson, A. J., Kilic, M., et al. 2012, ApJ, 760, 26
Barnes, R., & Heller, R. 2013, AsBio, 13, 279
Becker, J., Seligman, D. Z., Adams, F. C., & Styczinski, M. J. 2023, ApJL, 945, L24
Becklin, E. E., Farihi, J., Jura, M., et al. 2005, ApJL, 632, L119
Bédard, A., Bergeron, P., & Fontaine, G. 2017, ApJ, 848, 11
Belokurov, V., Penoyre, Z., Oh, S., et al. 2020, MNRAS, 496, 1922
Blackman, J., Danielski, C., Bachelet, E., et al. 2024, Confirmation of a Jovian Planet Analog Orbiting a White Dwarf, Rare Low-mass Neutron Star or Black Hole, JWST Proposal. Cycle 3, ID. #6078
Blackman, J. W., Beaulieu, J. P., Bennett, D. P., et al. 2021, Natur, 598, 272
Blouin, S., Dufour, P., & Allard, N. F. 2018a, ApJ, 863, 184
Blouin, S., Dufour, P., Allard, N. F., & Kilic, M. 2018b, ApJ, 867, 161
Blouin, S., & Xu, S. 2022, MNRAS, 510, 1059
Bonsor, A., Farihi, J., Wyatt, M. C., & van Lieshout, R. 2017, MNRAS, 468, 154
Bouchet, P., García-Marín, M., Lagage, P. O., et al. 2015, PASP, 127, 612
Brandt, T. D. 2018, ApJS, 239, 31
Brandt, T. D. 2021, ApJS, 254, 42
Chamandy, L., Blackman, E. G., Nordhaus, J., & Wilson, E. 2021, MNRAS, 502, L110
Charbonneau, D., Berta, Z. K., Irwin, J., et al. 2009, Natur, 462, 891
Chen, C. H., Su, K. Y. L., & Xu, S. 2020, NatAs, 4, 328
Cheng, S., Schlaufman, K., & Caiazzo, I. 2024, A Giant Planet Candidate Orbiting a Young, Massive White Dwarf, JWST Proposal. Cycle 3, ID. #6410
Choi, J., Dotter, A., Conroy, C., et al. 2016, ApJ, 823, 102
Chu, Y.-H., Su, K. Y. L., Bilikova, J., et al. 2011, AJ, 142, 75
Clayton, G. C., De Marco, O., Nordhaus, J., et al. 2014, AJ, 147, 142
Crane, J. D., Shectman, S. A., & Butler, R. P. 2006, Proc. SPIE, 6269, 626931
Crane, J. D., Shectman, S. A., Butler, R. P., et al. 2010, Proc. SPIE, 7735, 773553
Crane, J. D., Shectman, S. A., Butler, R. P., Thompson, I. B., & Burley, G. S. 2008, Proc. SPIE, 7014, 701479
Cunningham, T., Wheatley, P. J., Tremblay, P.-E., et al. 2022, Natur, 602, 219
Cutri, R. M., Skrutskie, M. F., van Dyk, S., et al. 2003, yCat, II/246
Debes, J., Sankrit, R., Fischer, T., et al. 2024, The Hubble Advanced Spectral Product (HASP) Program, Instrument Science Report COS 2024-01
Debes, J. H., & Sigurdsson, S. 2002, ApJ, 572, 556
Debes, J. H., Sigurdsson, S., & Woodgate, B. E. 2005, ApJ, 633, 1168
Debes, J. H., Walsh, K. J., & Stark, C. 2012, ApJ, 747, 148
Dotter, A. 2016, ApJS, 222, 8
Dufour, P., Blouin, S., Coutu, S., et al. 2017, in ASP Ser. 509, 20th European White Dwarf Workshop, ed. P. E. Tremblay, B. Gaensicke, & T. Marsh (San Francisco, CA: ASP), 3
Dufour, P., Kilic, M., Fontaine, G., et al. 2010, ApJ, 719, 803
Endl, M., & Williams, K. 2018, in The 21st European Workshop on White Dwarfs, 1, http://hdl.handle.net/2152/71591
Farihi, J., Becklin, E. E., & Zuckerman, B. 2008a, ApJ, 681, 1470

---

[26] https://waps.cfa.harvard.edu/MIST/

Farihi, J., Jura, M., Lee, J. E., & Zuckerman, B. 2010, ApJ, 714, 1386
Farihi, J., Jura, M., & Zuckerman, B. 2009, ApJ, 694, 805
Farihi, J., Zuckerman, B., & Becklin, E. E. 2008b, ApJ, 674, 431
Farihi, J., Hermes, J. J., Marsh, T. R., et al. 2022, MNRAS, 511, 1647
Foreman-Mackey, D. 2016, JOSS, 1, 24
Fortney, J. J., Marley, M. S., & Barnes, J. W. 2007, ApJ, 659, 1661
Fossati, L., Bagnulo, S., Haswell, C. A., et al. 2012, ApJL, 757, L15
Gaensicke, B. T., Debes, J. H., Dufour, P., et al. 2015, An HST legacy ultraviolet spectroscopic survey of the 13pc white dwarf sample, HST Proposal. Cycle 23, ID. #14076
Gaia Collaboration, Prusti, T., de Bruijne, J. H. J., et al. 2016, A&A, 595, A1
Gansicke, B. T., Marsh, T. R., Southworth, J., & Rebassa-Mansergas, A. 2006, Sci, 314, 1908
Gänsicke, B. T., Schreiber, M. R., Toloza, O., et al. 2019, Natur, 576, 61
Gentile Fusillo, N. P., Tremblay, P. E., Cukanovaite, E., et al. 2021, MNRAS, 508, 3877
Gillon, M., Jehin, E., Lederer, S. M., et al. 2016, Natur, 533, 221
Girven, J., Gansicke, B. T., Steeghs, D., & Koester, D. 2011, MNRAS, 417, 1210
Gomez Gonzalez, C. A., Wertz, O., Absil, O., et al. 2017, AJ, 154, 7
Gordon, K. D., Bohlin, R., Sloan, G. C., et al. 2022, AJ, 163, 267
Gaia Collaboration 2020, yCat, I/350
Hogg, M. A., Casewell, S. L., Wynn, G. A., et al. 2020, MNRAS, 498, 12
Holberg, J. B., Sion, E. M., Oswalt, T., et al. 2008, AJ, 135, 1225
Janson, M., Gratton, R., Rodet, L., et al. 2021a, Natur, 600, 231
Janson, M., Squicciarini, V., Delorme, P., et al. 2021b, A&A, 646, A164
Johnson, J. A., Morton, T. D., & Wright, J. T. 2013, ApJ, 763, 53
Johnson, J. A., Fischer, D. A., Marcy, G. W., et al. 2007, ApJ, 665, 785
Jura, M. 2003, ApJL, 584, L91
Jura, M., Farihi, J., & Zuckerman, B. 2007, ApJ, 663, 1285
Jura, M., Farihi, J., & Zuckerman, B. 2009, AJ, 137, 3191
Kervella, P., Arenou, F., Mignard, F., & Thévenin, F. 2019, A&A, 623, A72
Kilic, M., Brown, W. R., & McLeod, B. 2010, ApJ, 708, 411
Kilic, M., von Hippel, T., Leggett, S. K., & Winget, D. E. 2005, ApJL, 632, L115
Kilic, M., von Hippel, T., Leggett, S. K., & Winget, D. E. 2006, ApJ, 646, 474
Kiman, R., Xu, S., Faherty, J. K., et al. 2022, AJ, 164, 62
Klein, B., Jura, M., Koester, D., Zuckerman, B., & Melis, C. 2010, ApJ, 709, 950
Koester, D. 2009, A&A, 498, 517
Koester, D., Gänsicke, B. T., & Farihi, J. 2014, A&A, 566, A34
Koester, D., Voss, B., Napiwotzki, R., et al. 2009, A&A, 505, 441
Koester, D., & Wilken, D. 2006, A&A, 453, 1051
Koen, C., Kilkenny, D., van Wyk, F., & Marang, F. 2010, MNRAS, 403, 1949
Korol, V., Belokurov, V., & Toonen, S. 2022, MNRAS, 515, 1228
Kozakis, T., Kaltenegger, L., & Hoard, D. W. 2018, ApJ, 862, 69
Kozakis, T., Lin, Z., & Kaltenegger, L. 2020, ApJL, 894, L6
Lagos, F., Schreiber, M. R., Zorotovic, M., et al. 2021, MNRAS, 501, 676
Lagrange, A.-M., Bonnefoy, M., Chauvin, G., et al. 2010, Sci, 329, 57
Lai, S., Dennihy, E., Xu, S., et al. 2021, ApJ, 920, 156
Ledda, S., Danielski, C., & Turrini, D. 2023, A&A, 675, A184
Libby-Roberts, J. E., Berta-Thompson, Z. K., Désert, J.-M., et al. 2020, AJ, 159, 57
Limbach, M. A., Vanderburg, A., Stevenson, K. B., et al. 2022, MNRAS, 517, 2622
Limbach, M. A., Vanderburg, A., Blouin, S., et al. 2023, The MIRI survey for Exoplanets Orbiting White-dwarfs (MEOW), JWST Proposal. Cycle 2, ID. #3964
Limbach, M. A., MacDonald, R., Vanderburg, A., et al. 2024, Probing the Dynamical History and the Mid-IR SED of WD 1856b, JWST Proposal. Cycle 3, ID. #5204
Lindegren, L. 2024, Re-normalising the astrometric chi-square in Gaia DR2, GAIA-C3-TN-LU-LL-124-01, http://www.rssd.esa.int/doc_fetch.php?id=3757412
Lindegren, L., Klioner, S. A., Hernández, J., et al. 2021, A&A, 649, A2
Linder, E. F., Mordasini, C., Mollière, P., et al. 2019, AAP, 623, A85
Lloyd, J. P. 2011, ApJL, 739, L49
Loeb, A., & Maoz, D. 2013, MNRAS, 432, L11
Luhman, K. L., Burgasser, A. J., & Bochanski, J. J. 2011, ApJL, 730, L9
Luhman, K. L., Tremblin, P., Alves de Oliveira, C., et al. 2024, AJ, 167, 5
MacDonald, R. J. 2023, JOSS, 8, 4873
MacDonald, R. J., & Madhusudhan, N. 2017, MNRAS, 469, 1979
MacDonald, R. J., Batalha, N., Foote, T. O., et al. 2021, Under the Light of a Dead Star: Revealing the Atmospheric Composition of a White Dwarf Planet, JWST Proposal. Cycle 1, ID. #2358
Maldonado, R. F., Villaver, E., Mustill, A. J., & Chavez, M. 2022, MNRAS, 512, 104
Maldonado, R. F., Villaver, E., Mustill, A. J., Chávez, M., & Bertone, E. 2021, MNRAS, 501, L43
Marley, M. S., Saumon, D., Visscher, C., et al. 2021, ApJ, 920, 85
Masuda, K. 2014, ApJ, 783, 53
Melis, C., Farihi, J., Dufour, P., et al. 2011, ApJ, 732, 90
Merlov, A., Bear, E., & Soker, N. 2021, ApJL, 915, L34
Munoz, D. J., & Petrovich, C. 2020, ApJL, 904, L3
Mullally, F., Kilic, M., Reach, W. T., et al. 2007, ApJS, 171, 206
Mullally, F., Albert, L., Mullally, S. E., et al. 2024a, Confirmation of Planetary Companions to White Dwarf Stars, JWST Proposal. Cycle 3, ID. #4857
Mullally, S. E., Mullally, F., Albert, L., et al. 2021, A Search for the Giant Planets that Drive White Dwarf Accretion, JWST Proposal. Cycle 1, ID. #1911
Mullally, S. E., Debes, J., Cracraft, M., et al. 2024b, ApJL, 962, L32
Napiwotzki, R., Karl, C. A., Lisker, T., et al. 2020, A&A, 638, A131
Nielsen, E. L., De Rosa, R. J., Macintosh, B., et al. 2019, AJ, 158, 13
Nordhaus, J., & Spiegel, D. S. 2013, MNRAS, 432, 500
Paxton, B., Bildsten, L., Dotter, A., et al. 2011, ApJS, 192, 3
Paxton, B., Cantiello, M., Arras, P., et al. 2013, ApJS, 208, 4
Paxton, B., Marchant, P., Schwab, J., et al. 2015, ApJS, 220, 15
Poulsen, S., Debes, J., Farihi, J., et al. 2023, The MIRI Excess Around Degenerates Survey, JWST Proposal. Cycle 2, ID. #3964
Poulsen, S., Debes, J., Cracraft, M., et al. 2024, AJ, 167, 257
Reach, W. T., Kuchner, M. J., von Hippel, T., et al. 2005, ApJL, 635, L161
Rebassa-Mansergas, A., Solano, E., Xu, S., et al. 2019, MNRAS, 489, 3990
Reffert, S., Bergmann, C., Quirrenbach, A., Trifonov, T., & Künstler, A. 2015, A&A, 574, A116
Robert, A., Farihi, J., Van Eylen, V., et al. 2024, MNRAS, 533, 1756
Rogers, L. K., Debes, J., Anslow, R. J., et al. 2024, MNRAS, 527, 977
Sanderson, H., Bonsor, A., & Mustill, A. 2022, MNRAS, 517, 5835
Sigurdsson, S., Richer, H. B., Hansen, B. M., Stairs, I. H., & Thorsett, S. E. 2003, Sci, 301, 193
Smithsonian Astrophysical Observatory 2000, SAOImage DS9: A utility for displaying astronomical images in the X11 window environment, Astrophysics Source Code Library, ascl:0003.002
Sozzetti, A. 2005, PASP, 117, 1021
Stephan, A. P., Naoz, S., & Gaudi, B. S. 2021, ApJ, 922, 4
Stevenson, K. B. 2020, ApJL, 898, L35
Su, K. Y. L., Chu, Y. H., Rieke, G. H., et al. 2007, ApJL, 657, L41
Swan, A., Farihi, J., Su, K. Y. L., & Desch, S. J. 2024, MNRAS, 529, L41
Thorsett, S. E., Arzoumanian, Z., & Taylor, J. H. 1993, ApJL, 412, L33
Trierweiler, I. L., Doyle, A. E., & Young, E. D. 2023, PSJ, 4, 136
van der Walt, S., Colbert, S. C., & Varoquaux, G. 2011, CSE, 13, 22
van Sluijs, L., & Van Eylen, V. 2018, MNRAS, 474, 4603
Vanderbosch, Z., Hermes, J. J., Dennihy, E., et al. 2020, ApJ, 897, 171
Vanderburg, A., Becker, J. C., Daylan, T., et al. 2021, Thermal Emission from the First Planet Transiting a White Dwarf, JWST Proposal. Cycle 1, ID. #2507
Vanderburg, A., Johnson, J. A., Rappaport, S., et al. 2015, Natur, 526, 546
Vanderburg, A., Rappaport, S. A., Xu, S., et al. 2020, Natur, 585, 363
Vauclair, G., Schmidt, H., Koester, D., & Allard, N. 1997, A&A, 325, 1055
Venner, A., Limbach, M. A., Vanderburg, A., et al. 2023, Confirming a Giant Planet Around the White Dwarf GD 140, JWST Proposal. Cycle 2, ID. #3621
Venner, A., Vanderburg, A., & Pearce, L. A. 2021, AJ, 162, 12
Veras, D. 2021, Oxford Research Encyclopedia of Planetary Science (Oxford: Oxford Univ. Press), 1
Veras, D., Mustill, A. J., & Bonsor, A. 2024, RvMG, 90, 141
Veras, D., Mustill, A. J., Gänsicke, B. T., et al. 2016, MNRAS, 458, 3942
Vigan, A., Fontanive, C., Meyer, M., et al. 2021, A&A, 651, A72
Wenger, M., Ochsenbein, F., Egret, D., et al. 2000, A&AS, 143, 9
Werner, M. W., Roellig, T. L., Low, F. J., et al. 2004, ApJs, 154, 1
Xu, S., Dufour, P., Klein, B., et al. 2019, AJ, 158, 242
Xu, S., Jura, M., Pantoja, B., et al. 2015, ApJL, 806, L5
Yamaguchi, N., El-Badry, K., Fuller, J., et al. 2024, MNRAS, 527, 11719
Yang, H., & Ishiguro, M. 2015, ApJ, 813, 87
Zhan, R., Koll, D. D. B., & Ding, F. 2024, ApJ, 971, 125
Zhu, W., & Dong, S. 2021, ARAA, 59, 291
Zuckerman, B., & Becklin, E. E. 1987, Natur, 330, 138
Zuckerman, B., Melis, C., Klein, B., Koester, D., & Jura, M. 2010, ApJ, 722, 725